ADVANCED HEALTHCARE MATERIALS
www.advhealthmat.de

Protein Nanoparticles for Targeted SARS-CoV-2 Trapping and Neutralization

Marc Fornt-Suñé, Maria C. Puertas, Javier Martinez-Picado, Javier García-Pardo, and Salvador Ventura**

The coronavirus disease 2019 (COVID-19) pandemic, caused by the severe acute respiratory syndrome coronavirus 2 (SARS-CoV-2), continues to challenge global health despite widespread vaccination efforts, underscoring the need for innovative strategies to combat emerging infectious diseases effectively. Herein, LCB1-NPs and LCB3-NPs are engineered as a novel class of protein-only nanoparticles formed through coiled coil-driven self-assembly and tailored to interact specifically with the SARS-CoV-2 spike protein. The multivalency of LCB1-NPs and LCB3-NPs offers a strategy for efficiently targeting and neutralizing SARS-CoV-2 both in solution and when immobilized on surfaces. It is demonstrated that LCB1-NPs and LCB3-NPs bind to the SARS-CoV-2 spike protein's receptor-binding domain (RBD) with high affinity, effectively blocking the entry of SARS-CoV-2 virus-like particles into angiotensin-converting enzyme 2 (ACE2)-coated human cells. The cost-effectiveness, scalability, and straightforward production process of these protein nanoparticles make them suitable for developing novel anti-viral materials. Accordingly, it is shown how these nanostructures can be packed into columns to build up economic and highly potent trapping devices for SARS-CoV-2 adsorption.

1. Introduction

The coronavirus disease 2019 (COVID-19) pandemic caused by the severe acute respiratory syndrome coronavirus 2 (SARS-CoV-2) infected over 775 million people and caused more than 7 million deaths worldwide by April 2024.[1] The rapid spread of this emerging acute respiratory disease caught the health system and the scientific community off guard, resulting in devastating human, health, and economic consequences.[2–5] After a substantial scientific effort, vaccination was able to mitigate the massive and uncontrolled transmission of SARS-CoV-2,[6] but far from having disappeared, periodic outbreaks of the virus persist, and it may become a new cycling and seasonal pathogen.[7] Indeed, emerging sub-variants such as the JN.1, derived from the SARS-CoV-2 omicron strain, are currently spreading worldwide.[8,9] Altogether, the COVID-19 pandemic has warned of the dangers and consequences of emerging infectious

M. Fornt-Suñé, J. García-Pardo, S. Ventura
Institut de Biotecnologia i de Biomedicina (IBB)
Universitat Autònoma de Barcelona
Bellaterra 08193, Spain
E-mail: Javier.Garcia.Pardo@uab.cat; Salvador.Ventura@uab.cat

M. Fornt-Suñé, J. García-Pardo, S. Ventura
Departament de Bioquímica i Biologia Molecular
Universitat Autònoma de Barcelona
Bellaterra 08193, Spain

M. C. Puertas, J. Martinez-Picado
IrsiCaixa
Badalona 08916, Spain

M. C. Puertas, J. Martinez-Picado
Germans Trias i Pujol Research Institute (IGTP)
Badalona 08916, Spain

M. C. Puertas, J. Martinez-Picado
Biomedical Research Networking Center on Infectious Diseases (CIBERINFEC)
Madrid 28029, Spain

J. Martinez-Picado
Infectious Diseases and Immunity Department
University of Vic-Central University of Catalonia
Vic (UVic-UCC), Vic 08500, Spain

J. Martinez-Picado, S. Ventura
Catalan Institution for Research and Advanced Studies (ICREA)
Barcelona 08010, Spain

S. Ventura
Institut d'Investigació i Innovació Parc Taulí (I3PT CERCA)
Universitat Autònoma de Barcelona
Sabadell 08208, Spain

The ORCID identification number(s) for the author(s) of this article can be found under https://doi.org/10.1002/adhm.202402744

DOI: 10.1002/adhm.202402744

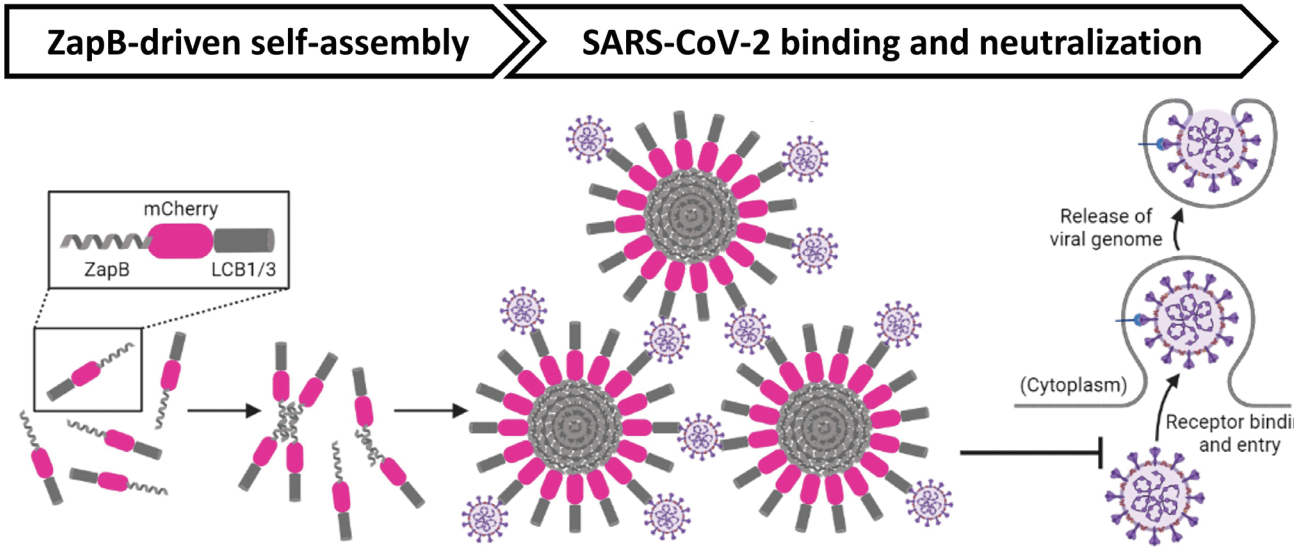

Figure 1. Graphical representation of the self-assembly and function of LCB1/LCB3-NPs. The fusion proteins ZapB-mCherry-LCB1 and ZapB-mCherry-LCB3 are separately overexpressed in *Escherichia coli* and intracellularly self-assemble into LCB1-NPs or LCB3-NPs as the protein monomers accumulate in the cytoplasm. Such protein nanoparticles are sustained by intermolecular coiled-coil interactions between the ZapB moieties of the different polypeptides. The preassembled protein nanoparticles, which can be easily and rapidly purified from the insoluble cell fraction, are red-fluorescent and display a high density of surface-exposed LCB1 and LCB3 domains that endow them with the capacity to bind the RBD of the SARS-CoV-2 spike protein specifically, thus capturing and neutralizing the viruses.

diseases and highlighted the need for new tools to combat them effectively and rapidly.

We have now acquired a comprehensive knowledge of the physiopathology and the molecular determinants that mediate SARS-CoV-2 infection of human cells.[10] The SARS-CoV-2 life cycle begins with host cell recognition through the interaction between the viral spike protein's receptor binding domain (RBD) and the human cell surface receptor angiotensin-converting enzyme 2 (ACE2). This highly specific interaction precedes the internalization of the virus and, therefore, is mandatory for SARS-CoV-2 replication in the target human cells.[11–14] Although ACE2 receptors on the ciliated cells of nasal epithelium and upper bronchial epithelia constitute the primary targets for SARS-CoV-2 during the early stages of infection, the presence of ACE2 receptors in other non-respiratory tissues such as small intestine, colon, kidney, heart muscle, testis, and thyroid gland has been associated with some complications arising from COVID-19.[2,11,15–18] Therefore, developing new agents capable of inhibiting the interaction between the spike protein and the ACE2 receptor has become a promising strategy to prevent and treat COVID-19.

Indeed, the SARS-CoV-2 spike protein is the main target for developing SARS-CoV-2 neutralizing antibodies (NAbs).[19] For instance, camelid-derived single-chain NAbs have been developed targeting the RBD domain of this trimeric protein.[20] Besides NAbs, a reduced number of nanostructured materials have also been designed to target specifically SARS-CoV-2 (Table S1, Supporting Information).[21–28]

In this study, we have engineered a new SARS-CoV-2 capturing material consisting of fluorescent protein-only nanoparticles that target the SARS-CoV-2 spike protein and block its interaction with the human ACE2 receptor. To generate this nanomaterial, we followed a modular approach that leverages the self-assembling properties of the protein ZapB. ZapB is a small 81-residue protein whose 3D structure comprises two α-helical polypeptide chains arranged in an anti-parallel orientation, forming a dimeric coiled-coil with a length of 116 Å. These ZapB dimers can further self-assemble into supramolecular structures, driven by a network of inter-dimer interactions near the α-helices termini.[29–32] In particular, we designed two tripartite fusion proteins (namely ZapB-mCherry-LCB1 and ZapB-mCherry-LCB3) consisting of ZapB as the self-assembling scaffolding module, the red fluorescent protein mCherry as a reporter, and either LCB1 or LCB3 proteins as the SARS-CoV-2 capturing moieties. LCB1 and LCB3 are two small (<8 kDa) proteins that bind to the RBD of the SARS-CoV-2 spike protein with picomolar affinity.[33,34] The contacts they establish are highly specific for SARS-CoV-2 since these domains do not recognize the related MERS-CoV S1S2 and SARS-CoV-1 S1S2 viruses.[35] Both LCB1 and LCB3 proteins were engineered from scratch using computer-assisted de novo design and they fold into a similar three-helix bundle.[34] We demonstrate that the recombinant expression of the ZapB-mCherry-LCB1 and ZapB-mCherry-LCB3 fusion proteins in microbial cell factories renders nanostructured protein nanoparticles, hereafter referred to as LCB1-NPs and LCB3-NPs, that exhibit red fluorescence and display LCB1 or LCB3 moieties at high density, thus having viral neutralizing activity (**Figure 1**). Importantly, the LCB1/LCB3-NPs can be easily and rapidly produced with high yields (>250 mg protein / L culture). As proof of concept, we show that LCB1/LCB3-NPs can be easily packed into columns that function as potent virus-capturing devices, highlighting the potential applicability of these protein nanoparticles in generating novel materials with SARS-CoV-2 antiviral properties.

2. Results and Discussion

2.1. Pre-Assembled LCB1-NPs and LCB3-NPs are Stable Fluorescent Protein Particles of Regular Round Shape and Submicrometric Size

Antibodies are one of the most efficient strategies for SARS-CoV-2 binding and neutralization. However, their development is typically complex, resource-intensive, and costly. In this study, we aimed to design and produce cost-effective protein-based nanoparticles that can target, capture, and neutralize SARS-CoV-2 viruses. These nanostructures constitute a versatile platform for the generation of novel antiviral materials. In this context, we have engineered ZapB-mCherry-LCB1 and ZapB-mCherry-LCB3 fusion proteins that were individually overexpressed in *Escherichia coli* (*E. coli*). As the recombinant proteins reach the bacterial cytoplasm, ZapB drives their spontaneous assembly into LCB1-NPs and LCB3-NPs through coiled coil-mediated intermolecular interactions. Because mCherry and LCB1/LCB3 are sequentially linked to ZapB in the fusion proteins, these functional globular domains will also be integrated into the α-helical coiled coil-based scaffolds, providing red-fluorescent nanoparticles with a high density of surface-exposed SARS-CoV-2 capturing moieties. While the red fluorescence emitted by mCherry is useful for particle tracking, the LCB1 and LCB3 moieties should confer the nanoparticles the ability to target the RBD of the SARS-CoV-2 spike protein. As shown in Figure S1 (Supporting Information), pre-assembled LCB1-NPs and LCB3-NPs were successfully purified from the insoluble cell fractions following a fast and straightforward procedure.

Pure samples of LCB1-NPs and LCB3-NPs were analyzed using Scanning Electron Microscopy (SEM) to observe the nanoparticle morphology. As shown in **Figures 2a** and **3a**, both LCB1-NPs and LCB3-NPs exhibited a regular rounded morphology and a submicrometric size. We performed a size distribution analysis by measuring the nanoparticles spotted in different SEM micrographs, rendering average sizes of 739.03 ± 42.74 and 731.52 ± 49.32 nm for LCB1-NPs and LCB3-NPs, respectively (Figure S5, Supporting Information). The size range observed in the SEM micrographs is consistent with Dynamic Light Scattering (DLS) measurements of the same LCB1-NPs and LCB3-NPs dispersed in a buffered solution, which reported a hydrodynamic diameter of 722.6 ± 168.5 and 746.4 ± 139.2 nm, respectively (Figures 2b and 3b).

The proper folding of the different globular domains in the modular protein nanoparticles is a fundamental requirement for preserving their functionality. LCB1-NPs and LCB3-NPs are essentially sustained by native α-helical coiled-coil interactions that should not alter the conformation of their constituent globular proteins.[36] Supporting this, LCB1-NPs and LCB3-NPs exhibit intense red fluorescence, with excitation and emission spectra matching those of native mCherry (Figures 2c,d and 3c,d). Furthermore, secondary structure analysis by Fourier Transform Infrared Spectroscopy (FTIR) revealed a predominant band at 1650 cm^{-1} for both LCB1-NPs and LCB3-NPs assignable to the native α-helical folds of the ZapB, LCB1, and LCB3 domains (Figures 2e and 3e).

To further support the native arrangement of the different domains in the tripartite fusions, we conducted structural predictions for both the ZapB-mCherry-LCB1 and ZapB-mCherry-LCB3 proteins using AlphaFold 2. As depicted in Figure S2 (Supporting Information), ZapB moieties are predicted to form α-helical domains, with high confidence, reinforcing the hypothesis that the nanoparticles are stabilized by native α-helical coiled-coil interactions between these domains during self-assembly. Additionally, LCB1 and LCB3 were predicted to form small globular α-helical domains, which aligns well with the FTIR data. As expected, the modeled structures in both cases indicated that the mCherry fluorescent moiety retains its typical beta-barrel structure in the fusion.

As a control, we also produced and purified protein nanoparticles consisting of the ZapB-mCherry modules but lacking the SARS-CoV-2 capturing moieties (hereafter CTL-NPs). Their biophysical characterization by SEM, DLS, Fluorescence Spectroscopy, and FTIR revealed comparable traits with respect to LCB1-NPs and LCB3-NPs (Figure S3, Supporting Information).

Before engaging in functional assays, we monitored the stability of LCB1-NPs, LCB3-NPs, and CTL-NPs under the specific solution conditions required for these assays. We incubated the nanoparticles at a concentration of 2.5 μM in 50 mM Tris-HCl, pH 7.4, containing 100 mM NaCl at 25 °C with constant agitation for five days. During this period, we monitored the particles size using DLS (Figure S4a–c, Supporting Information). No significant changes in the size of LCB1-NPs, LCB3-NPs, or CTL-NPs were observed, indicating that the nanoparticles remain colloidally stable under these conditions. Additionally, we collected aliquots of the nanoparticles daily for analysis by SDS-PAGE. The results showed that the different nanoparticles remained unaltered over time, showing no signs of proteolysis (Figure S4d, Supporting Information).

2.2. LCB1-NPs and LCB3-NPs Bind to the SARS-CoV-2 Spike Protein RBD

Next, we have evaluated the ability of LCB1/LCB3-NPs to bind to the SARS-CoV-2 spike protein RBD. First, we dispersed LCB1-NPs, LCB3-NPs, and CTL-NPs in a physiological buffer and incubated them in suspension with recombinantly expressed RBD of the SARS-CoV-2 spike protein tagged with the yellow fluorescent protein (YFP-RBD). Then, binding was evaluated using confocal microscopy and fluorescence spectroscopy. As shown in **Figure 4a**, confocal microscopy images revealed that samples containing LCB1-NPs and LCB3-NPs showed colocalized red fluorescence from mCherry and yellow fluorescence from YFP, indicative of YFP-RBD binding. In contrast, CTL-NPs, lacking the SARS-CoV-2 capturing moieties, showed only red fluorescence, thus ruling out any possible non-specific binding of YFP-RBD to the protein nanoparticles scaffold. To further explore the co-localization of LCB1-NPs and LCB3-NPs with YFP-RBD, we performed intensity profile analyses of high-magnification images, examining the fluorescence intensity across regions of interest (ROI) for both the RBD signal (YFP in green) and the LCB1/LCB3-NPs (mCherry in red) (Figure 4b). While LCB1 and LCB3-NPs are entirely composed of ZapB-mCherry-LCB1/LCB3 fusion proteins, only the surface-exposed domains are readily accessible and capable of capturing YFP-RBD. Consequently, YFP fluorescence from the captured RBD is predominantly de-

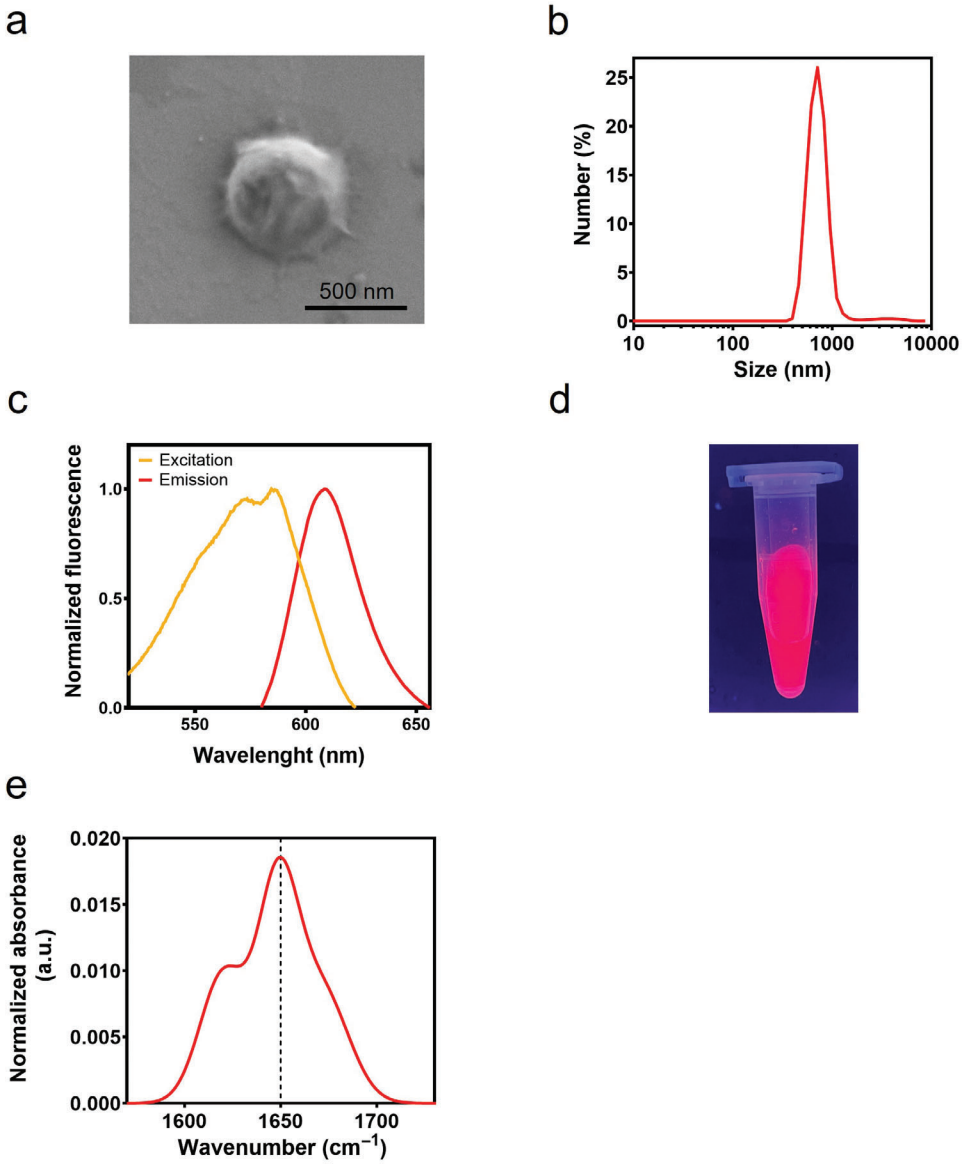

Figure 2. Biophysical characterization of LCB1-NPs. a) Scanning Electron Microscopy image of an individual LCB1-NP. b) Size distribution of a suspension of LCB1-NPs determined by Dynamic Light Scattering. c) Fluorescence excitation (yellow) and emission (red) spectra of LCB1-NPs recorded by Fluorescence Spectroscopy. d) Image of LCB1-NPs dispersed in a buffered solution and emitting red fluorescence when exposed to UV light. e) Secondary structure determination of LCB1-NPs by Fourier Transform Infrared Spectroscopy.

tected at the nanoparticle surfaces, while red fluorescence is more evenly distributed within the nanoparticles. This fluorescence pattern reflects the spatial distribution of the functional domains, with the RBD-binding activity localized primarily at the surface of the NP, as expected. Again, no co-localization pattern was evident for CTL-NPs devoid of LCB1/LCB3 domains. These observations are in good agreement with fluorescence spectroscopy analysis of the same samples (Figure 4c), which showed that LCB1-NPs and LCB3-NPs exhibited both mCherry and YFP signals. As expected, CTL-NPs showed only mCherry fluorescence.

2.3. Nitrocellulose-Immobilized LCB1-NPs and LCB3-NPs Bind to the SARS-CoV-2 Spike Protein RBD

As demonstrated above, the LCB1-NPs and LCB3-NPs dispersed in a buffered solution can bind to the SARS-CoV-2 spike protein RBD. We further evaluated whether their binding activity remains intact when immobilized on a surface using dot blot assays. We deposited increasing amounts of LCB1-NPs, LCB3-NPs, and CTL-NPs onto nitrocellulose membranes that were further incubated with a solution containing YFP-RBD. After washing out unbound YFP-RBD, the membranes were imaged for

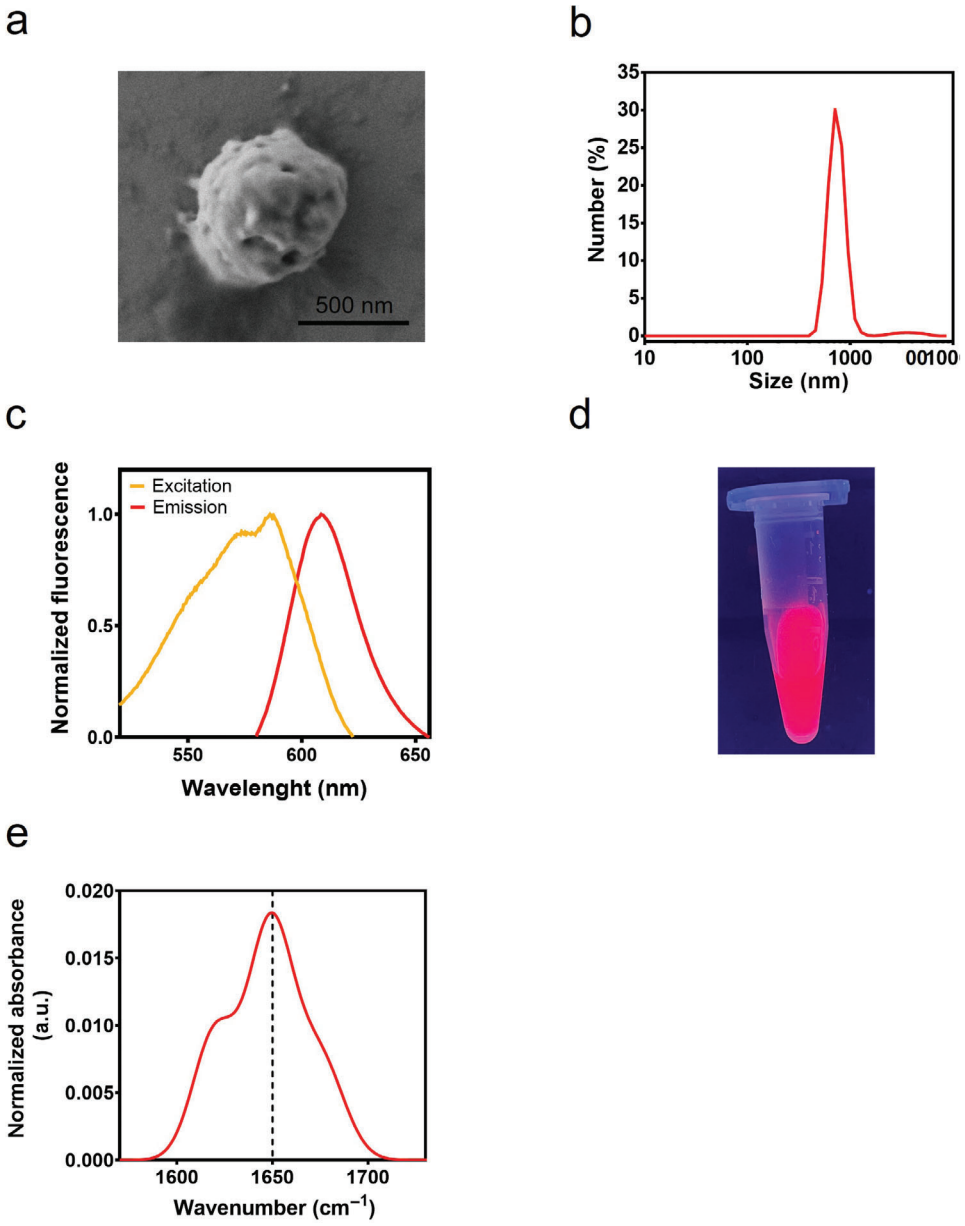

Figure 3. Biophysical characterization of LCB3-NPs. a) Scanning Electron Microscopy image of an individual LCB3-NP. b) Size distribution of a suspension of LCB3-NPs determined by Dynamic Light Scattering. c) Fluorescence excitation (yellow) and emission (red) spectra of LCB3-NPs recorded by Fluorescence Spectroscopy. d) Image of LCB3-NPs dispersed in a buffered solution and emitting red fluorescence when exposed to UV light. e) Secondary structure determination of LCB3-NPs by Fourier Transform Infrared Spectroscopy.

mCherry and YFP fluorescent signals. As shown in **Figure** 5a, both LCB1-NPs and LCB3-NPs efficiently captured the YFP-RBD protein, as evidenced by the colocalization of the mCherry and YFP fluorescence. Conversely, CTL-NPs presented only red fluorescence from mCherry, which ultimately demonstrates the lack of unspecific binding of YFP-RBD to the nanoparticles' protein scaffold.

Additionally, we quantified fluorescent signals from the dot blot membranes and observed that LCB1-NPs and LCB3-NPs exhibit a clear concentration-dependent increase in the YFP-RBD fluorescence (Figure 5b,c). Notably, the YFP-RBD fluorescence showed a linear correlation with the amount of LCB1-NPs or LCB3-NPs immobilized on the surface. Next, the affinity of LCB1-NPs and LCB3-NPs for the YFP-RBD protein was quantitatively evaluated. We deposited a constant quantity of LCB1-NPs, LCB3-NPs, and CTL-NPs on different nitrocellulose membranes and incubated them with growing concentrations of YFP-RBD protein. As shown in Figure 5d–f, again, a dose-dependent increase in the YFP-RBD fluorescence was observed for both the LCB1-NPs and LCB3-NPs, with characteristic saturation curves and estimated half maximal effective concentration (EC50) values of 58.9 ± 17.0 and 129.5 ± 49.4 nM, respectively.

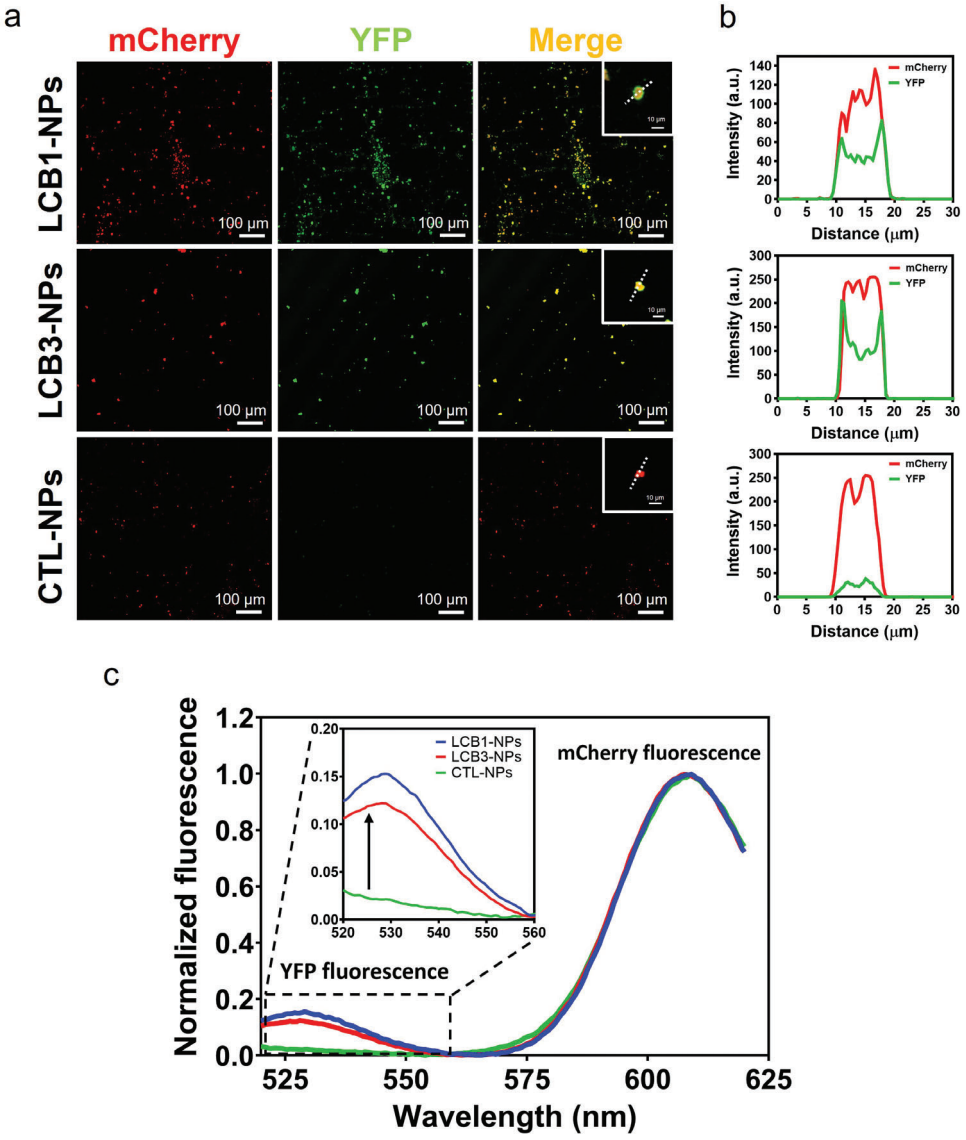

Figure 4. Binding of YFP-RBD protein to LCB1-NPs, LCB3-NPs, and CTL-NPs. a) Confocal Microscopy images of LCB1-NPs (up), LCB3-NPs (middle), and CTL-NPs (bottom) after incubation with a solution of YFP-RBD protein. The left panels show the mCherry fluorescence (in red) corresponding to the nanoparticles. The central panels show the YFP fluorescence (in green) attributed to the particle-bound YFP-RBD. The right panels show the merge of both mCherry and YPF-RBD fluorescence channels (in yellow). The insets show a magnification of the merged images. The regions of interest (ROI) used for further co-localization analyses are shown as white dashed lines. b) Intensity profile analyses of the ROI shown in (a) as white dashed lines. These results are representative of three independent measurements. c) Fluorescence spectroscopy emission spectra of the same samples containing LCB1-NPs (blue), LCB3-NPs (red), and CTL NPs (green), after incubation with a solution of YFP-RBD protein. The YFP fluorescence emission spectra can be observed between 520 and 560 nm. The mCherry fluorescence emission spectra can be observed between 570 and 625 nm.

2.4. LCB1-NPs and LCB3-NPs Efficiently Block the Binding of the SARS-CoV-2 Spike Protein to the Human ACE2 Receptor

The initial stage of SARS-CoV-2 entry into host cells involves the binding of its trimeric spike proteins to the human ACE2 receptor. We evaluated the ability of LCB1-NPs and LCB3-NPs to compete and interfere with the interaction between the RBD of the SARS-CoV-2 spike protein and the human ACE2 receptor. We used a bioluminescent immunoassay (see **Figure** 6a and Materials and Methods section for details), which quantifies the levels of spike RBD-ACE2 receptor interaction using a luciferase reporter system. In the presence of neutralizing entities, the luminescent signal diminishes in a manner that is proportional to the potency of the RBD binder, since it competes with the RBD-ACE2 interaction, thereby hindering the reconstitution of luciferase.

As shown in Figure 6b, LCB1-NPs and LCB3-NPs efficiently inhibited the interaction between the RBD of the SARS-CoV-2 spike protein and the human ACE2 receptor, with calculated half maximal inhibitory concentrations (IC50) of 26.06 and 54.06 nM respectively. Remarkably, no inhibitory effect was observed for CTL-NPs lacking the SARS-CoV-2 capturing moieties, underscoring the specificity of the LCB1-NPs and LCB3-NPs.

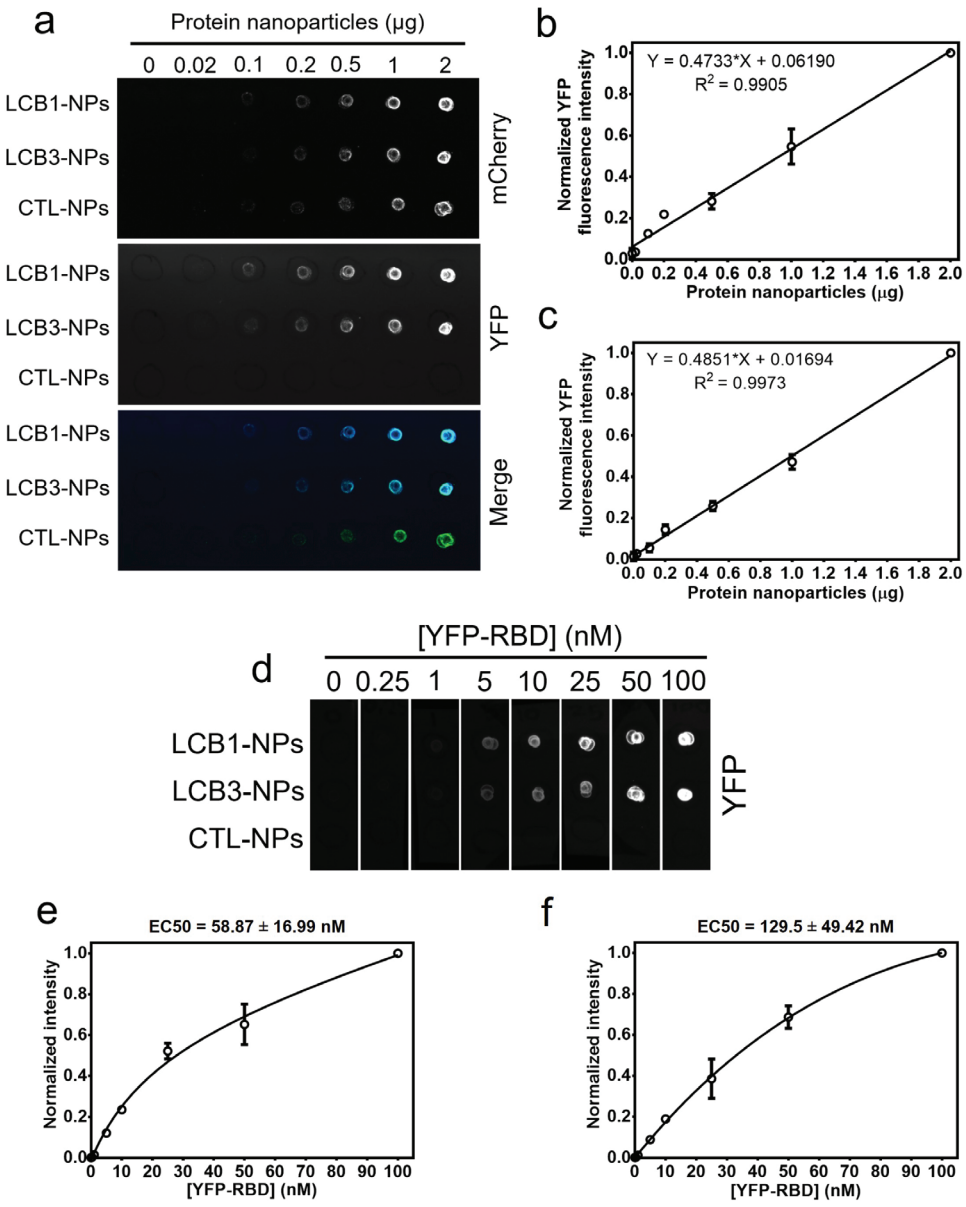

Figure 5. Binding of YFP-RBD protein to LCB1-NPs, LCB3-NPs, and CTL-NPs immobilized on nitrocellulose membranes. a) Dot blots showing the binding of YFP-RBD to surface-immobilized LCB1-NPs, LCB3-NPs, and CTL-NPs. The top panel shows the mCherry fluorescence (mCherry) corresponding to the protein nanoparticles. The central panel shows the YFP-RBD fluorescence (YFP) corresponding to the captured YFP-RBD protein. The bottom panel shows the merge of both mCherry and YFP-RBD fluorescent signals (blue). b,c) Dose-response curves corresponding to the YFP fluorescence captured by increasing amounts of surface-immobilized LCB1-NPs (b) and LCB3-NPs (c). The data were obtained by analyzing the fluorescence intensities from panel a. d) Dot blot membranes with a fixed quantity of immobilized LCB1-NPs, LCB3-NPs, and CTL-NPs after incubation with increasing concentrations of YFP-RBD. e,f) Dose-response curves obtained from the quantification of the YFP fluorescent signals displayed by the YFP-RBD protein captured by immobilized LCB1-NPs (e) or LCB3-NPs (f) from the dot blot membranes in panel d. The assays corresponding to panels a-c and d-f have been performed in triplicate ($n = 3$). Data is shown as mean ± standard deviation.

All in all, our results indicated that LCB1-NPs and LCB3-NPs can block the binding of SARS-CoV-2 spike RBD to its receptor. This opens new possibilities for utilizing these protein nanoparticles in material applications, including surface functionalization, diagnostic assays, and as active components of viral adsorption systems.

2.5. LCB1-NPs and LCB3-NPs Inhibit the Entry of SARS-CoV-2 Virus-Like Particles into ACE2-Coated Human Cells

In previous sections, we demonstrated that LCB1-NPs and LCB3-NPs effectively capture the spike protein's RBD. More importantly, we have shown that LCB1-NPs and LCB3-NPs can block

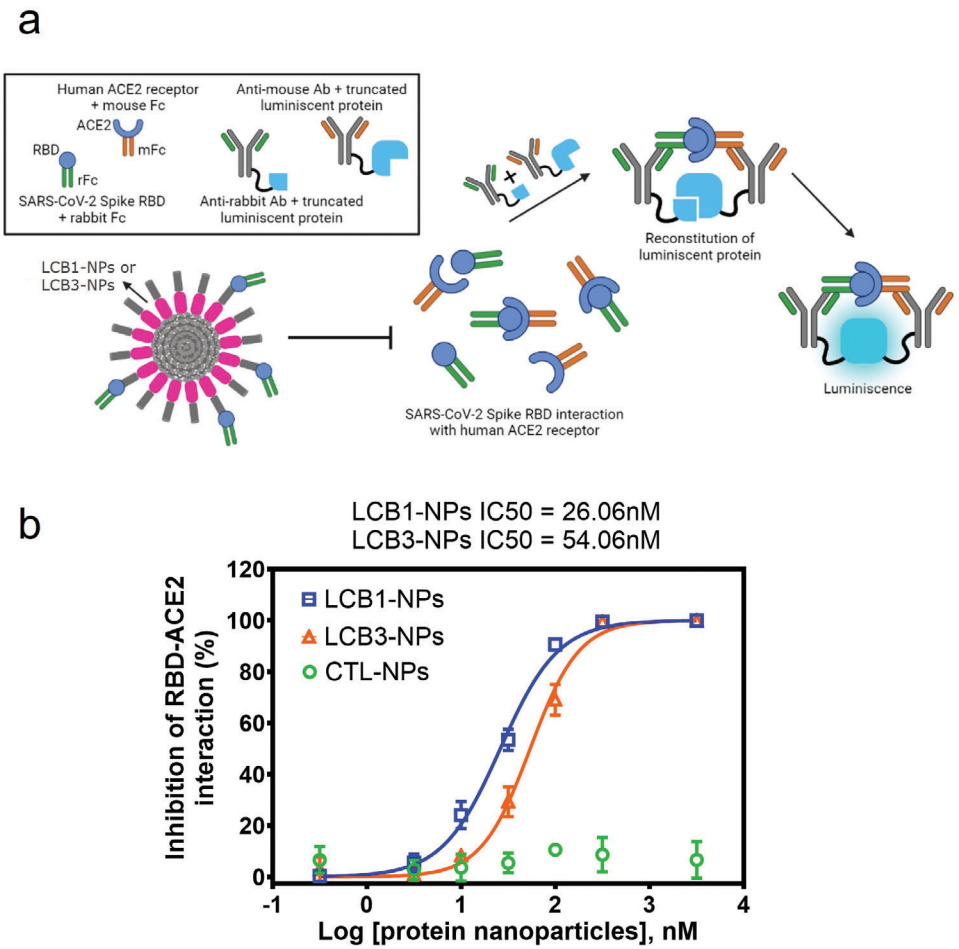

Figure 6. Inhibition of the SARS-CoV-2 Spike RBD-ACE2 receptor interaction by LCB1-NPs and LCB3-NPs. a) Schematic illustration of the principle of the implemented bioluminescent immunoassay Lumit. b) Inhibition of the RBD-ACE2 interaction by increasing amounts of LCB1-NPs, LCB3-NPs, and CTL-NPs. Each concentration was assayed in at least duplicate ($n = 2$). Data is presented as mean ± standard deviation.

the interaction between the spike protein RBD and the human ACE2 receptor with high potency. It is widely accepted that blocking this interaction would exert a viral neutralizing effect.

To demonstrate the performance of LCB1-NPs and LCB3-NPs as SARS-CoV-2 neutralizing agents, we employed the HiBiT luminescence assay.[37,38] This recently developed technology uses non-infectious SARS-CoV-2 pseudotyped virus-like particles (SC2-VLPs) containing the HiBiT fragment and engineered human ACE2-HEK293T cells that stably express ACE2 receptors at its surface and the LgBiT fragment in their cytosol. Upon spike-ACE2 interaction, the SC2-VLPs fuse with the cellular membrane, releasing HiBiT into target cells. This causes the binding of the HiBiT moiety to LgBiT, which generates a strong luminescent signal in the presence of its specific substrate.[38] As illustrated in **Figure** 7a, the active molecules that interfere with SARS-CoV-2 entry to host cells block the entry/fusion processes of SC2-VLPs, thereby preventing HiBiT-LgBiT complementation and luminescence production.

Consistent with the above-described data, when increasing concentrations of the LCB1-NPs and LCB3-NPs were used, we observed a concentration-dependent decrease in the measured luminescent signal. This indicates that LCB1-NPs and LCB3-NPs effectively neutralize the SC2-VLPs and block their cellular internalization with a calculated IC50 of 1.12 and 1.75 nM, respectively (Figure 7b). It is worth mentioning that the VLPs used in this approach contain the full-length SARS-CoV-2 spike protein (i.e., the G614 variant). This demonstrates that the LCB1-NPs and LCB3-NPs bind to the RBD domain and effectively block the binding of the SARS-CoV-2 spike protein to its receptor, with an IC50 much lower than that reported for other SARS-CoV-2 neutralizing nanomaterials, like cellular nanosponges[21] or chitosan-based nanoparticles[22] (see, also Table S1, Supporting Information).

Furthermore, a direct comparison of the IC50 values obtained for the LCB1-NPs and LCB3-NPs in the in vitro Lumit assays (Figure 6) and the VLPs neutralization assays (Figure 7), reveals that both protein nanoparticles are significantly more efficient in blocking internalization into host cells as compared to the in vitro RBD binding inhibition. Indeed, a 23-fold and 30-fold increase was observed for LCB1-NPs and LCB3-NPs, respectively. This enhanced efficiency can be explained by the multivalent nature of LCB1-NPs and LCB3-NPs, which are designed to display a high density of spike-capturing moieties on their surfaces. Consequently, each nanoparticle can concurrently bind multi-

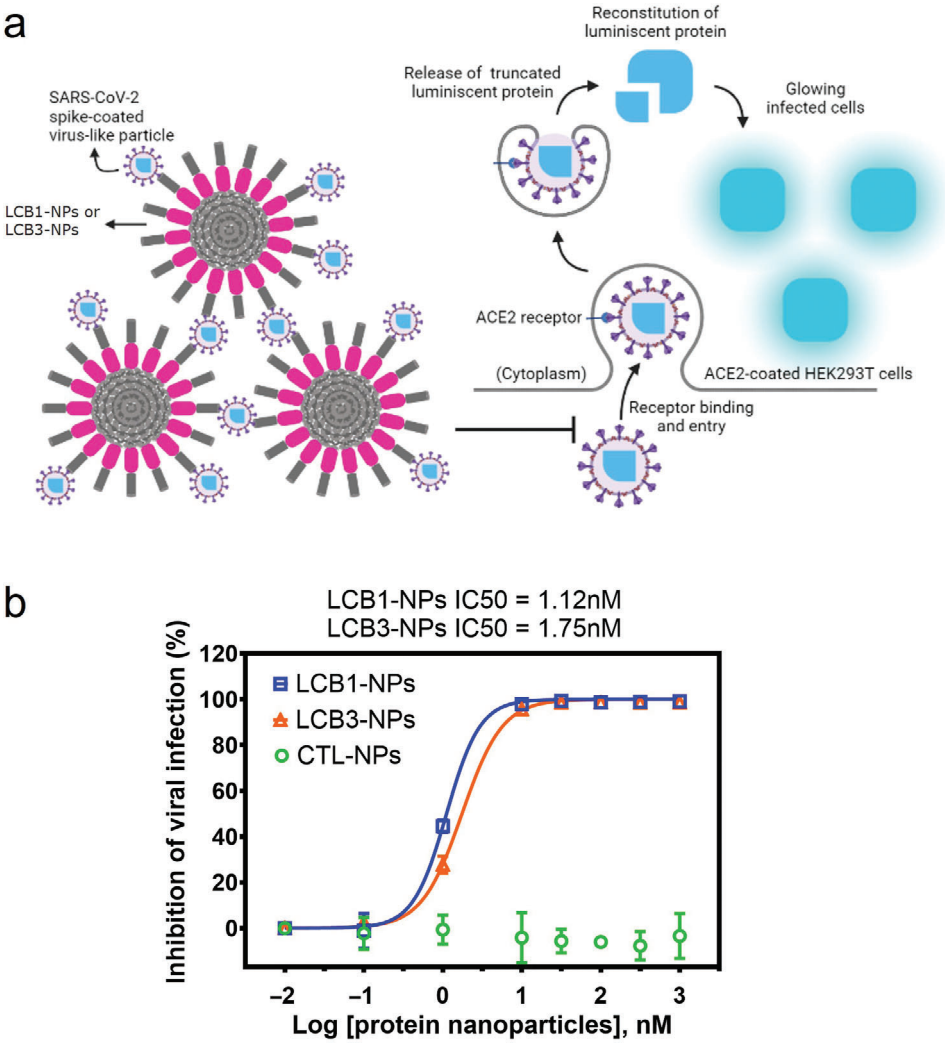

Figure 7. Inhibition of viral infection of human cells by LCB1-NPs and LCB3-NPs. a) Schematic illustration of the principle of the implemented cellular assay. b) Inhibition of viral infection of human cells by increasing amounts of LCB1-NPs, LCB3-NPs, and CTL-NPs. Data is shown as mean ± standard deviation ($n = 4$).

ple spike proteins, especially when assayed with VLPs that are densely coated with SARS-CoV-2 spike proteins.

2.6. SARS-CoV-2-Trap Columns Engineered with LCB1-NPs and LCB3-NPs Capture High Viral Loads

A crucial aspect of the fight against a pandemic is delivering a rapid response; thus, preformulated tools to speedily develop efficient viral adsorbing materials can be transformative in curbing virus transmission, particularly in a context where wastewater and sewage from COVID-19 patients' secretions and excretions have been found to contain substantial quantities of infective SARS-CoV-2 particles,[39] which can remain viable for up to 7 days in solution and contribute to viral spread.[40]

We envisioned that packing the LCB1/LCB3-NPs into chromatography columns could provide a potent SARS-CoV-2 capturing device (**Figure 8**). When designing the different fusion proteins that constitute the LCB1/LCB3-NPs, a histidine tag was incorporated at the end of each sequence. Leveraging this feature, we conducted a proof of concept by mixing 1.75 mg of histidine-tagged LCB1-NPs, LCB3-NPs, or CTL-NPs with NTA-Ni agarose beads as a matrix. The mixture was then packed into polypropylene chromatography columns and washed extensively with sterile PBS (Figure S6, Supporting Information). An additional mock column containing the NTA-Ni agarose matrix but no nanoparticles was also prepared. This negative control was used to demonstrate that the matrix itself cannot retain SARS-CoV-2 viruses. To gauge the functionality of these trapping devices, high loads of replication-competent SARS-CoV-2 virus, equivalent to those found in nasopharyngeal swabs from acutely infected patients, were flowed through the columns. The retention capacity of the engineered SARS-CoV-2-capturing columns was assessed by performing q-PCR analysis and infectivity assays on the eluate (Figure 8a). We used the SARS-CoV-2 reference strain BavPat1/2020 expanded and titrated in Vero E6 cells.

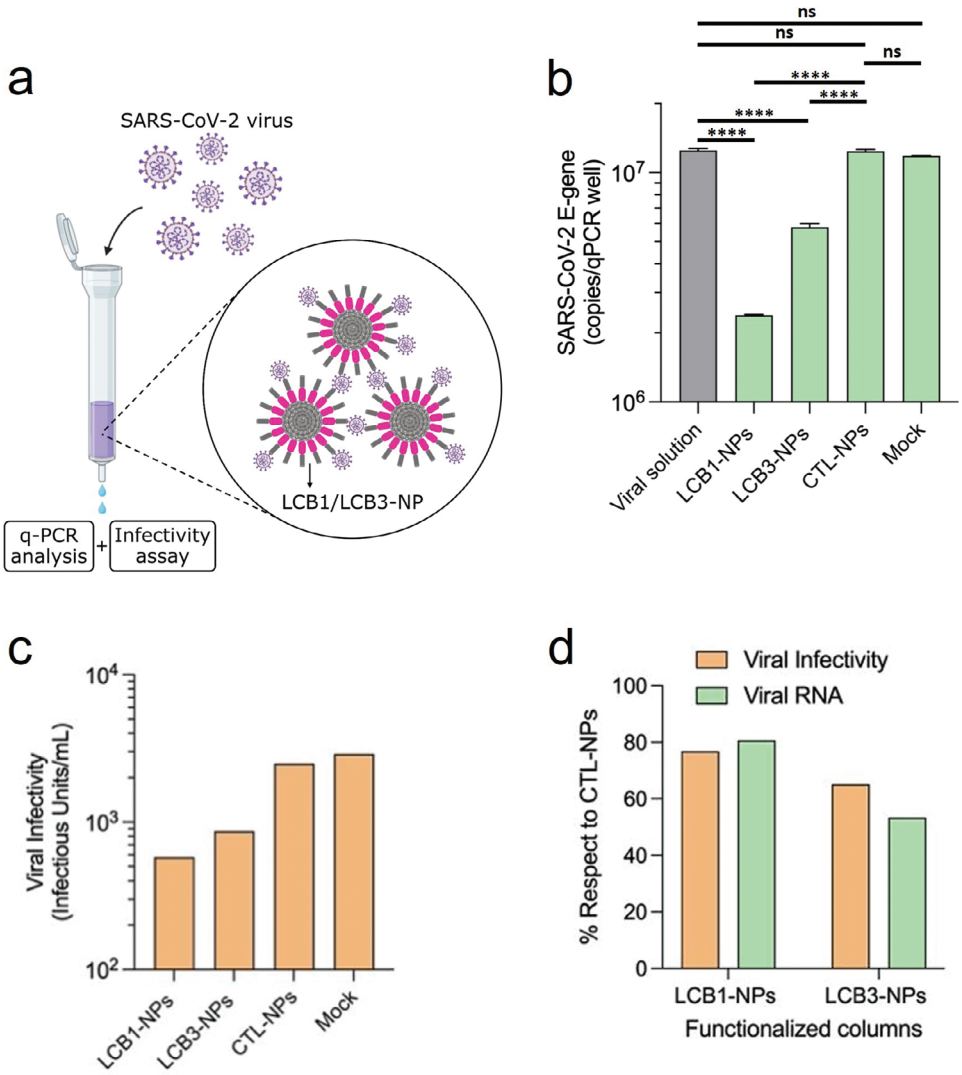

Figure 8. Retention of replication-competent SARS-CoV-2 virus by the filtering devices engineered with LCB1-NPs and LCB3-NPs. a) Schematic depiction of the experimental pipeline. A high SARS-CoV-2 viral titer is loaded into a filtering device functionalized with LCB1-NPs or LCB3-NPs. Then, the sample that exits the column is analyzed by q-PCR and infectivity assays. b) Levels of viral RNA in the samples eluted from the columns as quantified by qPCR. Data is shown as mean ± standard deviation ($n = 2$ independent qPCR measurements, see Experimental Section for details). ****p <0.0001. Statistical analysis was performed using ordinary one-way ANOVA and post hoc multiple comparisons analysis using the Tukey test. c) Infectivity of the samples eluted from the columns tested in VeroE6 cell cultures. d) Percentage of SARS-CoV-2 virus retained in the filtration devices calculated from the infectivity assays (orange) and from the qPCR analysis (green).

According to q-PCR analysis, columns functionalized with LCB1-NPs and LCB3-NPs significantly reduced the amount of viral RNA in the samples, capturing 80% and 55% of the loaded virus, respectively (Figure 8b,d). In contrast, neither the mock columns nor those containing CTL-NPs were effective, with comparable levels of SARS-CoV-2 RNA in the samples before and after passage through these columns (Figure 8b). In excellent agreement, we observed a reduction in viral infectivity on Vero E6 cells by 4.3-fold and 2.9-fold, corresponding to SARS-CoV-2 retention values of 77% and 65% for LCB1-NPs and LCB3-NPs, respectively (Figure 8c,d).

There have been several previous attempts to develop SARS-CoV-2 capturing devices, including ultrafiltration systems, which are well suited to isolate and concentrate viral particles from liquid samples.[41] However, this approach is not specific and often requires high operational pressures and sophisticated equipment. Magnetic particles, conjugated with an anti-Coronavirus spike antibody, are also used for SARS-CoV-2 immunoprecipitation from body fluids and in vitro expression systems. While this is a rapid and reliable approach for viral enrichment, its application is limited to micro-scale systems due to both the cost of production and the limited availability of specific antibodies. More recently, SARS-CoV-2 adsorbing columns have been developed by immobilizing a peptide designed based on the sequence of hACE2 on Toray fiber.[42] This technology, however, is expensive and time-consuming, as it requires the use of non-natural amino acids, post-synthesis PEGylation of the peptides, and a chemical reaction to link the peptide to the support covalently. Consider-

ing this, LCB1-NPs and LCB3-NPs represent a very promising protein-only anti-SARS-CoV-2 nanomaterial system. This system is broadly applicable for both micro- and macro-scale preparation and can be used for viral removal and/or concentration from water sources and/or biologically relevant samples.

3. Conclusion

In this research, we have engineered LCB1-NPs and LCB3-NPs, a novel self-assembling material consisting of regular, round-shaped, submicrometric, and fluorescent protein nanoparticles capable of specifically binding and neutralizing SARS-CoV-2 viruses. These protein nanoparticles are constructed from ZapB-mCherry-LCB1 and ZapB-mCherry-LCB3 tripartite fusion proteins. The ZapB protein drives their spontaneous self-assembly through coiled-coil interactions to build protein nanoparticles that are functionalized with a fluorescent tracer and SARS-CoV-2 capturing moieties.

The various SARS-CoV-2 neutralizing materials developed thus far (Table S1, Supporting Information) exhibit significant differences in composition, size, and neutralizing potency. These variations do not necessarily make one material superior to another but rather indicate that they are suitable for different applications. For instance, different functional nanostructured materials and their derived technologies, such as polymer-based nanocomposites, have been applied for the development of face masks with high particulate filtration and rapid inactivation of SARS-CoV-2.[28] These systems are specifically designed to block and inactivate viruses on surfaces and rely primarily on the antiviral properties of synthetic polymers and/or metals.

Among the advantages of our new nanostructured material, we highlight its easy, fast, and high-yield production and purification process. LCB1-NPs and LCB3-NPs spontaneously self-assemble when the respective fusion proteins are expressed in *E. coli* and their purification from the insoluble fraction of the cells only requires successive detergent washes. In addition to the simplicity and potential scalability of this process, it is highly cost-effective. For instance, producing nanoparticles sufficient for 10 SARS-CoV-2-trap columns, as those described in the previous section, costs less than 1 euro, including all necessary reagents for production and purification.

Significantly, LCB1-NPs and LCB3-NPs demonstrate efficient viral neutralization, making them promising nanomaterials for developing SARS-CoV-2 diagnostic assays, surface functionalization, or fabrication of viral adsorbing devices. We have demonstrated the high affinity and specificity of LCB1-NPs and LCB3-NPs for the SARS-CoV-2 virus, showing that they can be deposited onto a surface or packed into columns while preserving their virus-capturing properties. As each LCB1-NPs and LCB3-NPs is composed of many copies of their respective fusion protein, they are fully coated with SARS-CoV-2 binders, resulting in a high density of SARS-CoV-2 binding sites per particle. This multivalency, provides the nanoparticles with increased avidity in comparison to other formulations containing only a single recognition module per molecule, thus making LCB1-NPs and LCB3-NPs exceptionally potent SARS-CoV-2 binders.

Our design of LCB1-NPs and LCB3-NPs employs a genetically encoded modular protein engineering approach, allowing for easy addition or removal of functional modules to customize the nanoparticles' function for diverse applications. This flexibility enables the material to be re-engineered to target other pathogens by integrating the appropriate recognition module into the fusion protein. This provides a robust framework for the generation of new materials to combat potential future emerging infectious diseases effectively and rapidly, particularly when leveraged with recent advancements in de novo protein design.[43,44]

4. Experimental Section

Production and Purification of the Protein Nanoparticles: ZapB-mCherry-LCB1, ZapB-mCherry-LCB3, and ZapB-mCherry DNA sequences were cloned separately into pET-28a(+) vectors. For the obtention of LCB1-NPs, LCB3-NPs, and CTL-NPs, *Escherichia coli* BL21 (DE3) (Invitrogen, Waltham, USA) competent cells were transformed respectively with the different DNA constructs and the cells were grown in 20 mL of Luria-Bertani broth supplemented with 50 µg mL^{-1} kanamycin. The cultures were maintained at 37 °C under constant agitation 250 rpm until reaching an optical density at 600 nm of 0.6 a.u. Then, protein expression was induced with 1 mM Isopropyl β-D-1-thiogalactopyranoside (ITPG, Thermo Fisher Scientific, USA) for 6 h under agitation at 250 rpm and 30 °C. Afterward, the cells were recovered by centrifuging the cultures at 2500 rcf for 20 min at 4 °C. The samples were frozen and stored at −80 °C until use.

For the purification of LCB1-NPs, LCB3-NPs, and CTL-NPs, the cell pellets were defrosted and resuspended in 1 mL of buffer A (50 mM Tris-HCl, 100 mM NaCl, pH 7.4) supplemented with 1 mM phenylmethylsulphonyl fluoride (PMSF, Sigma-Aldrich Corporation, USA) and 150 µg mL^{-1} lysozyme (Sigma–Aldrich Corporation, USA). The cell suspension was incubated for 1 h under agitation at 37 °C, and subsequently sonicated using a Branson digital sonifier 450 (Branson Ultrasonics Corporation, USA) for 3 min at 15% amplitude and 1 s cycles while kept cold on ice. Then, 10 µL of Nonidet P40 Substitute (Sigma–Aldrich Corporation, USA) were added to the cell lysate and incubated for 1 h under agitation at 4 °C. Next, the mixture was supplemented with 30 µL of 1 M $MgSO_4$ and 25 µL of 1 mg mL^{-1} DNAse I (Sigma–Aldrich Corporation, USA) and was incubated for 1 h under agitation at 37 °C. Afterward, the sample was centrifuged for 20 min at 15 000 rcf and 4 °C. The resulting protein nanoparticle-containing pellet was washed thrice with 500 µL of buffer A containing 0.5% Triton X-100 and one additional washing step was performed with 500 µL of buffer A containing 2% Triton X-100. Finally, the last washing step was performed with buffer A to remove remnants of detergent. After centrifugation, the samples were resuspended in buffer A to obtain pure LCB1-NPs, LCB3-NPs, and CTL-NPs. The final protein concentration was determined by measuring the absorbance at 280 nm of the final purified nanoparticles prepared in 6 M guanidine hydrochloride using a Specord 200 Plus Spectrophotometer (Analytik Jena, Jena, Germany).

Dynamic Light Scattering (DLS): Size determination of LCB1-NPs, LCB3-NPs, and CTL-NPs was performed by DLS using a Zetasizer Nano S90 (Malvern Panalytical, Malvern, UK). The protein nanoparticles were prepared at a concentration of 25 µM in 50 mM Tris-HCl, pH 7.4, containing 100 mM NaCl. For each sample, a set of 12 repeated measures was recorded at 25 °C. As for tracking the size of the protein nanoparticles over-time, aliquots of 2.5 µM LCB1-NPs, LCB3-NPs, and CTL-NPs were prepared in 50 mM Tris-HCl, pH 7.4, containing 100 mM NaCl and 0.01% sodium azide. They were incubated for 5 days at 25 °C under constant agitation in a rotating wheel. The mean hydrodynamic diameter of the nanoparticles was measured every 24 h by DLS using a Zetasizer Nano S90 (Malvern Panalytical, Malvern, UK). Additionally, an aliquot of each sample was taken daily for an SDS-PAGE analysis of the nanoparticles over time.

Scanning Electron Microscopy (SEM): The morphology of LCB1-NPs, LCB3-NPs, and CTL-NPs was analyzed by SEM. The protein nanoparticles were suspended in 50 mM Tris-HCl, pH 7.4, containing 100 mM NaCl. The samples were deposited on silicon chip specimen supports for SEM viewing (Ted Pella Inc., Redding, USA), and subsequently dried with N2 flow.

All the samples were observed in a Field Emission Merlin Scanning Electron Microscope (Zeiss Merlin, Oberkochen, Germany) operating at an acceleration voltage of 1 kV and employing the in lens secondary electron detector.

The diameter of 36 protein nanoparticles identified in each set of SEM micrographs corresponding to LCB1-NPs and LCB3-NPs were measured using the ImageJ software[45] and used to perform size distribution analysis.

Fourier Transform Infrared Spectroscopy (FTIR): The secondary structure of LCB1-NPs, LCB3-NPs, and CTL-NPs was assessed by FTIR using a Bruker Tensor 27 FTIR (Bruker Optics, Billerica, USA) supplied with a Specac Golden Gate MKII ATR accessory. The protein nanoparticles were diluted in 50 mM Tris-HCl, pH 7.4 buffer with 100 mM NaCl and were placed on the ATR crystal. The samples were completely dried with a N2 flow. Each acquired spectrum comprised 32 scans measured at a resolution of 1 cm^{-1} within the 1800–1500 cm^{-1} range. The spectral data were processed and normalized using the OPUS MIR Tensor 27 software (Bruker Optics, Billerica, USA), and fitted and deconvoluted using PeakFit Software (Systat Software).

Confocal Microscopy: For confocal microscopy experiments, three suspensions containing 150 µL of 5 µM LCB1-NPs, LCB3-NPs, and CTL-NPs were separately incubated with 25 nM YFP-RBD protein for 1 h at room temperature. During the incubation time, the samples were resuspended every 10 min to allow an efficient particle-ligand interaction. Next, the three samples were centrifuged at 15 000 rcf and 4 °C for 20 min, and the pellets were resuspended in 150 µL of 50 mM Tris-HCl, pH 7.4, containing 100 mM NaCl to remove the unbound YFP-RBD. After a second centrifugation step, the samples were resuspended in 50 µL of 50 mM Tris-HCl, pH 7.4 buffer, containing 100 mM NaCl. Afterward, 5 µL of each sample were placed on top of a microscopy glass slide, covered with a coverslip, and confocal microscopy images were obtained with Leica SP5 confocal microscope (Leica Microsystems, Germany) at the excitation/emission wavelengths for both YFP and mCherry. The fluorescent signals from the YFP present in the YFP-RBD protein and from the mCherry present in the protein nanoparticles were imaged using the Imaris software (Oxford Instruments, UK). The intensity profile analyses reporting on the fluorescence intensity across the indicated regions of interest (ROI) in the high-resolution magnification insets were performed using ImageJ software.[45]

Fluorescence Spectroscopy: The samples prepared for confocal microscopy imaging were also analyzed by fluorescence spectroscopy. As described above for confocal microscopy experiments, LCB1-NPs, LCB3-NPs, and CTL-NPs were incubated with a YFP-RBD solution and washed to remove unbound YFP-RBD. Next, aliquots of the different samples were analyzed in a Jasco FP-8200 fluorescence spectrofluorometer (Jasco Corporation, Japan). The samples were excited at 505 nm and the resulting fluorescence emission spectra were recorded from 520 to 620 nm acquiring three accumulations at medium sensitivity. The emission and excitation bandwidths were set at 5 nm, data interval at 0.5 nm, response at 0.5 s, and scan speed at 1000 nm min^{-1}.

For measuring the fluorescence excitation and emission spectra of mCherry present in the protein nanoparticles, 50 µL samples of 25 µM LCB1-NPs, LCB3-NPs, and CTL-NPs were separately prepared in buffer A (50 mM Tris pH 7.4 and 100 mM NaCl). Next, the samples were measured in a Jasco FP-8200 fluorescence spectrofluorometer (Jasco Corporation, Japan) using the following settings: high sensitivity, excitation and emission bandwidths at 5 nm, response at 0.5 s, data interval at 0.5 nm, scan speed at 1000 nm min^{-1}, and 5 accumulations. The measurement range was 480–680 nm for excitation spectra (excitation mode and emission wavelength: 690 nm) and 580–690 nm for emission spectra (emission mode and excitation wavelength: 570 nm).

Dot Blot Analysis: For the initial dose-response experiments, the following amounts of LCB1-NPs, LCB3-NPs, and CTL-NPs were deposited on a nitrocellulose membrane. The samples were placed on three separate rows of evenly spaced dots containing increasing nanoparticle concentrations (i.e., 0, 0.02, 0.1, 0.2, 0.5, 1, and 2 µg). The different spots were prepared by adding a total volume of 6 µL to each spot. Three different replicate membranes were prepared. After the spots were dried, the membranes were blocked with a 5% bovine serum albumin (BSA) solution for 1 h. The membranes were washed with PBS containing 0.1% Tween 20 for 15 min. Afterward, the membranes were incubated in a PBS solution containing 25 nM of SARS-CoV-2 spike RBD protein labeled with yellow fluorescent protein (YFP-RBD) for 1 h. The purified YFP-RBD protein was obtained as described by Behbahanipour et al., 2023.[37] Finally, the membranes were washed in PBS containing 0.1% Tween 20 for 15 min to eliminate remnants of non-captured YFP-RBD. All incubations were performed at room temperature and under mild agitation.

For the saturation experiments eight nitrocellulose membranes containing three dots of 2 µg of LCB1-NPs, LCB3-NPs, and CTL-NPs were prepared similarly as described above. Briefly, the membranes were blocked in a 5% bovine serum albumin (BSA) solution for 1 h and washed in PBS containing 0.1% Tween 20 for 15 min. The membranes were incubated with different YFP-RBD solutions containing increasing ligand concentrations. (i.e., 0, 0.25, 1, 5, 10, 25, 50, and 100 nM). After incubation, the membranes were washed in PBS containing 0.1% Tween 20 for 15 min to eliminate remnants of non-captured YFP-RBD. All incubations were performed at room temperature and under mild agitation to allow an optimal ligand interaction. All the resulting dot blot membranes were imaged using a ChemiDoc MP Imaging System (Bio-Rad Laboratories Inc., Hercules, USA) set for multiplex fluorescence detection system. The acquired images were analyzed with Image Lab Software (Bio-Rad Laboratories Inc., Hercules, USA). Volume analysis and local background subtraction method were implemented to quantify the signal coming from each dot and build dose-response and saturation curves. All the experiments were performed in triplicate.

Lumit SARS-CoV-2 Spike RBD: hACE2 Immunoassay: To evaluate the capacity of LCB1-NPs, LCB3-NPs, and CTL-NPs to block the in vitro interaction between the RBD of the SARS-CoV-2 Spike protein and its human receptor hACE2, the Lumit Bioluminescent Immunoassay (Promega, Madison, USA) was performed following the instructions provided by the supplier.[38] In essence, this immunoassay implements a SARS-CoV-2 spike RBD protein fused to the constant Fc region of a rabbit antibody (r-RBD), a human ACE2 receptor fused to the constant Fc region of a mouse antibody (m-ACE2), and a couple of anti-rabbit and anti-mouse secondary antibodies that are each one fused to one half of a truncated bioluminescent enzyme (Figure 6). Under normal conditions, the viral RBD protein and the human ACE2 receptor interact, which allows that the anti-rabbit and anti-mouse secondary antibodies respectively bind to the Fc regions of r-RBD and m-ACE2 and the two halves of the truncated enzyme are brought close together enough to reconstitute the fully functional enzyme that will emit a luminescent signal in the presence of its substrate. However, in the presence of blocking particles, they compete with the binding of m-ACE2 to r-RBD and thus disrupt the RBD-ACE2 interaction, resulting in a decrease of the detected luminescent signal. To perform the experiments, growing concentrations of LCB1-NPs, LCB3-NPs, and CTL-NPs (0.3, 3, 9.48, 30, 94.86, 300, and 3000 nM) were incubated with SARS-CoV-2 Spike RBD protein for 30 min in a 96 well MaxiSorp microwell plate (436 110, Thermo Fisher Scientific, USA). Then, the human receptor hACE2 and the Lumit antibody mix were added to the mixture and incubated for 1 h. Finally, the Lumit detection reagent was added and incubated for 30 min to generate a bioluminescent signal that is directly proportional to the levels of interaction between the RBD of the SARS-CoV-2 Spike protein and its human receptor hACE2 in each well of the plate. These bioluminescent signals were measured in a Spark plate reader (Tecan, Männedorf, Switzerland) set to luminescence mode. All the mentioned incubations were performed at room temperature and three replicate assays were performed simultaneously for each analyzed protein nanoparticle concentration. The obtained relative luminescence data were normalized to 100% and converted into their complementary counterpart, which is the % of inhibition of the interaction between the SARS-CoV-2 Spike RBD and the human ACE2 receptor.

SARS-CoV-2 HiBiT-PsVLP Viral Neutralization Assay: To evaluate the capacity of LCB1-NPs, LCB3-NPs, and CTL-NPs to neutralize the infection of SARS-CoV-2 spike-coated pseudotyped virus-like particles to human cells presenting ACE2 receptors on the membrane, the SARS-CoV-2 HiBiT-PsVLP Assay (Promega, Madison, USA) was performed following the instructions provided by the supplier.[38] First, growing concen-

trations of LCB1-NPs, LCB3-NPs, and CTL-NPs (0.01, 0.1, 1, 10, 31.62, 100, 316.22, and 1000 nM) were incubated with SARS-CoV-2 spike-coated pseudotyped virus-like particles for 30 min in a 96 well cell culture plate (83.3924, SARSTEDT, Germany). Next, HEK293T(LgBiT) cells coated with hACE2 receptors were incubated in DMEM supplemented with FBS and DrkBiT peptide for 15 min and then were added to mixture and incubated for 3 h. Finally, the Nano-Glo live cell reagent was added and incubated for 15 min to generate a luminescent signal that is directly proportional to the levels of viral infection to the human HEK293T (LgBiT) cells that are found in each well of the plate. These luminescent signals were measured in a Spark plate reader (Tecan, Männedorf, Switzerland) set to luminescence mode. All the incubations were performed at 37 °C in a CO_2 incubator and three replicates of each condition were performed. The resultant luminescence data was normalized and converted into % of inhibition of viral infection compared to control condition.

Preparation of SARS-CoV-2-Trap Columns: LCB1-NPs, LCB3-NPs, and CTL-NPs were dispersed in buffer A (50 mM Tris pH 7.4 and 100 mM NaCl) at a final concentration of 10 μg μL^{-1}. Afterward, 1.75 mg of each nanoparticle suspension was separately mixed with Ni-NTA agarose beads as scaffolding matrix (Ref. R90115, ThermoFisher Scientific, USA) to a final volume of 1 mL. The final samples (1 mL each) were packed into 2 mL Polyprep Chromatography Columns (Ref. 7 311 550, BioRad, USA). One mock column was also prepared by packing 1 mL of Ni-NTA agarose beads devoid of any protein nanoparticles. The columns were placed vertically, and the nanoparticle-containing resin was left to settle by gravity for 1 h at room temperature. The four virus filtering devices were equilibrated by flowing 10 mL of PBS through each of the columns by gravity. The whole process was performed in a laminar airflow cabinet to ensure sterility. All the utilized material was sterile under and pyrogen free. Additionally, the protein nanoparticle suspensions and the empty polypropylene chromatography columns were initially irradiated under a UV light source. All the utilized buffers were sterilized by filtration with 0.22 μM filters.

SARS-CoV-2 Trapping Assay: SARS-CoV-2 reference strain Bav-Pat1/2020 was obtained from Universitätsmedizin Berlin (CUB) via EVAg network. The viral isolate was then expanded and titrated in Vero E6 cells (ATCC, CRL-1586).

Five volumes of culture media (DMEM-HPA Capricorn Scientific, supplemented with 100 U mL^{-1} penicillin and 100 mg mL^{-1} streptomycin) was used to equilibrate the columns before addition of the virus. The viral stock was diluted 1/20 in culture media (to a final concentration of 8×105 SARS-Cov-2 E-gene RNA copies/μL) just before filtration. Each column was charged with 3 mL of the resulting SARS-CoV-2 suspension and filtered by gravity. The first 1.1 mL of the eluted fraction, which contain the equilibration media, were discarded and the next 2 mL were collected for further analysis.

To measure the retention ability of the columns, the concentration of virus in the resulting eluates was measured by qPCR. After RNA isolation using the QIAamp Viral RNA Mini Kit (Qiagen), the E_Assay Fist Line Screening (IDT) and TaqManTM Fast Virus 1-Step Master Mix (Applied Biosystems, 4 444 434) was used to quantify the number of SARS-CoV-2 genomes by qPCR on the 7500 RealTime System (Applied Biosystems) as previously described.[46] Serial dilutions of the 2019-nCoV_E Positive Control (IDT) were included in the qPCR assay to infer the number of viral genomes in the samples. Data is shown as mean ± standard deviation (n = 2 independent qPCR measurements/experiments). Statistical analysis was conducted using GraphPad Prism 10 software (GraphPad Software Inc.), performing an ordinary one-way ANOVA test followed by post hoc multiple comparisons analysis using the Tukey test. $p < 0.01$ considered statistically significant.

To measure the infectivity potential remaining at the column eluates, their infection capacity were monitored by an endpoint dilution assay in Vero E6 cells. Briefly, Vero E6 cells were seeded at 20.000 cells per well in a 96-well plate. The day later, 100 μL of each eluate, and six further serial dilutions 1/5, all of them prepared in culture media, were used to infect Vero E6 cultures in triplicate. After 48 h, cytopathic effect was directly visualized in the cell cultures and infectious units per mL calculated based on the Reed and Muench method.[47]

Statistical Analysis: All experiments were performed at least in triplicate, with the exception of Figure 8b,c, where a different number of replicates was analyzed, as indicated. Please note that in the qPCR analyses, n = 2 was used. In this experiment, two different controls were included: control nanoparticles (CNT-NPs) and a mock column without nanoparticles. Additionally, two SARS-CoV-2 virus-trapping nanoparticle systems were evaluated (LCB1-NPs and LCB3-NPs). In all cases, data are presented as mean ± standard deviation (SD). Plotting and statistical analysis were performed using GraphPad Prism 10 software (GraphPad Software Inc.). The statistical analysis for Figure 8b was conducted using one-way ANOVA followed by post hoc multiple comparisons using the Tukey test. *p < 0.01 was considered statistically significant, and ****$p < 0.0001$.

Artificial Intelligence Statement: The authors declare that they have not used any type of generative artificial intelligence for the writing of this manuscript, nor for the creation of images, graphics, tables, or their corresponding captions.

Supporting Information

Supporting Information is available from the Wiley Online Library or from the author.

Acknowledgements

This work was funded by the Spanish Ministry of Science and Innovation (PID2022-137963OB-I00), by ICREA, ICREA-Academia 2020, to S.V. This work was also funded by the CERCA Programme (Generalitat de Catalunya) to S.V. M.F.-S. was supported by the Spanish Ministry of Science and Innovation (FPU20/0 2897). J.G-P. was supported by the Spanish Ministry of Science and Innovation with a Juan de la Cierva Incorporación IJC2019-041039-I. J.M-P. was supported by the Spanish Ministry of Science and Innovation (grants PID2022-139271OB-I00 and CB21/13/00063, Spain), Fundació La Marató de TV3 (grant 202120-30-31-32, Spain), and the crowd funding initiative YoMeCorono. The authors greatly appreciate the technical support in electron microscopy and confocal imaging provided by the members of the Microscopy Service of the Universitat Autònoma de Barcelona. The authors would also like to express the gratitude to Imma Ratera and Marc Martínez-Miguel for their advice in nanoparticle surface immobilization assays.

Conflict of Interest

The authors declare no conflict of interest.

Author Contributions

J.G.-P. and S.V. designed the conceptual framework of the present study. M.F.-S., J.G.-P. and S.V. designed the experimental framework involving the production and characterization of the described protein-based nanomaterials, the validation of their function, the assessment of binding affinities, and the engineering of the SARS-CoV-2-trap columns. M.C.P. and J.M.-P. designed the experimental framework involving the SARS-CoV-2 trapping assays using the engineered SARS-CoV-2-trap columns, and the analysis of the eluates by qPCR and infectivity assays. M.F.-S., J.G.-P., and M.C.P., performed the experiments. M.F.-S., J.G.-P., and S.V. wrote the manuscript with the valuable comments from all authors.

Data Availability Statement

The data that support the findings of this study are available in the supplementary material of this article.

Keywords

antiviral nanomaterials, coiled coil protein nanoparticles, SARS-CoV-2, SARS-CoV-2 trapping, viral neutralization

Received: September 4, 2024
Revised: September 27, 2024
Published online:

[1] "COVID-19 deaths | WHO COVID-19 dashboard,", can be found under https://data.who.int/dashboards/covid19/cases.
[2] B. Hu, H. Guo, P. Zhou, Z.-L. Shi, *Nat. Rev. Microbiol.* **2021**, *19*, 141.
[3] COVID-19 Mental Disorders Collaborators, *Lancet* **2021**, *398*, 1700.
[4] D. M. Altmann, E. M. Whettlock, S. Liu, D. J. Arachchillage, R. J. Boyton, *Nat. Rev. Immunol.* **2023**, *23*, 618.
[5] A. D. Kaye, C. N. Okeagu, A. D. Pham, R. A. Silva, J. J. Hurley, B. L. Arron, N. Sarfraz, H. N. Lee, G. E. Ghali, J. W. Gamble, H. Liu, R. D. Urman, E. M. Cornett, *Best Pract. Res. Clin. Anaesthesiol.* **2021**, *35*, 293.
[6] D. H. Barouch, *N. Engl. J. Med.* **2022**, *387*, 1011.
[7] W. S. Byun, S. W. Heo, G. Jo, J. W. Kim, S. Kim, S. Lee, H. E. Park, J.-H. Baek, *Environ. Res.* **2021**, *196*, 110972.
[8] "Tracking SARS-CoV-2 variants,", can be found under https://www.who.int/activities/tracking-SARS-CoV-2-variants.
[9] P. V. Markov, M. Ghafari, M. Beer, K. Lythgoe, P. Simmonds, N. I. Stilianakis, A. Katzourakis, *Nat. Rev. Microbiol.* **2023**, *21*, 361.
[10] D. A. Jamison, S. Anand Narayanan, N. S. Trovão, J. W. Guarnieri, M. J. Topper, P. M. Moraes-Vieira, V. Zaksas, K. K. Singh, E. S. Wurtele, A. Beheshti, *Eur. J. Hum. Genet. EJHG* **2022**, *30*, 889.
[11] C. B. Jackson, M. Farzan, B. Chen, H. Choe, *Nat. Rev. Mol. Cell Biol.* **2022**, *23*, 3.
[12] M. Hoffmann, H. Kleine-Weber, S. Schroeder, N. Krüger, T. Herrler, S. Erichsen, T. S. Schiergens, G. Herrler, N.-H. Wu, A. Nitsche, M. A. Müller, C. Drosten, S. Pöhlmann, *Cell* **2020**, *181*, 271.
[13] X. Ou, Y. Liu, X. Lei, P. Li, D. Mi, L. Ren, L. Guo, R. Guo, T. Chen, J. Hu, Z. Xiang, Z. Mu, X. Chen, J. Chen, K. Hu, Q. Jin, J. Wang, Z. Qian, *Nat. Commun.* **2020**, *11*, 1620.
[14] M. Letko, A. Marzi, V. Munster, *Nat. Microbiol.* **2020**, *5*, 562.
[15] J. H. Ahn, J. Kim, S. P. Hong, S. Y. Choi, M. J. Yang, Y. S. Ju, Y. T. Kim, H. M. Kim, M. T. Rahman, M. K. Chung, S. D. Hong, H. Bae, C.-S. Lee, G. Y. Koh, *J. Clin. Invest.* **2021**, *131*, e148517.
[16] Y. Wang, Y. Wang, W. Luo, L. Huang, J. Xiao, F. Li, S. Qin, X. Song, Y. Wu, Q. Zeng, F. Jin, Y. Wang, *Int. J. Med. Sci.* **2020**, *17*, 1522.
[17] X. Zou, K. Chen, J. Zou, P. Han, J. Hao, Z. Han, *Front. Med.* **2020**, *14*, 185.
[18] F. Liu, X. Long, B. Zhang, W. Zhang, X. Chen, Z. Zhang, *Clin. Gastroenterol. Hepatol. Off. Clin. Pract. J. Am. Gastroenterol. Assoc.* **2020**, *18*, 2128.
[19] Y. Chen, X. Zhao, H. Zhou, H. Zhu, S. Jiang, P. Wang, *Nat. Rev. Immunol.* **2023**, *23*, 189.
[20] M. Bhattacharya, S. Chatterjee, S.-S. Lee, C. Chakraborty, *Int. J. Biol. Macromol.* **2023**, *229*, 70.
[21] Q. Zhang, A. Honko, J. Zhou, H. Gong, S. N. Downs, J. H. Vasquez, R. H. Fang, W. Gao, A. Griffiths, L. Zhang, *Nano Lett.* **2020**, *20*, 5570.
[22] A. Mali, G. Franci, C. Zannella, A. Chianese, S. Anthiya, A. M. López-Estévez, A. Monti, A. De Filippis, N. Doti, M. J. Alonso, M. Galdiero, *Pharmaceutics* **2023**, *15*, 1621.
[23] Y. Guo, W. Song, Y. Dong, X. Wang, G. Nie, F. Li, *Nano Lett.* **2024**, *24*, 3614.
[24] M. Sun, S. Liu, T. Song, F. Chen, J. Zhang, J.-A. Huang, S. Wan, Y. Lu, H. Chen, W. Tan, Y. Song, C. Yang, *J. Am. Chem. Soc.* **2021**, *143*, 21541.
[25] J. Zhang, Y. Xu, Y. Huang, M. Sun, S. Liu, S. Wan, H. Chen, C. Yang, Y. Yang, Y. Song, *J. Am. Chem. Soc.* **2022**, *144*, 13146.
[26] J. D. D. P. de Moraes Segundo, J. S. F. Constantino, G. B. Calais, C. F. de Moura Junior, M. O. S. de Moraes, J. H. L. da Fonseca, J. Tsukamoto, R. R. D. C. Monteiro, F. K. Andrade, M. A. d'vila, C. W. Arns, M. M. Beppu, R. S. Vieira, *Polymers* **2022**, *14*, 4157.
[27] W. T. Lam, T. S. Babra, J. H. D. Smith, M. C. Bagley, J. Spencer, E. Wright, B. W. Greenland, *Polymers* **2022**, *14*, 4172.
[28] W. Ahmed, A. H. Al-Marzouqi, M. H. Nazir, T. A. Rizvi, E. Zaneldin, M. Khan, *Int. J. Mol. Sci.* **2022**, *23*, 11235.
[29] M. Gil-Garcia, S. Ventura, *Acta Biomater.* **2021**, *131*, 472.
[30] M. Gil-Garcia, S. Navarro, S. Ventura, *Microb. Cell Fact.* **2020**, *19*, 117.
[31] G. Ebersbach, E. Galli, J. Møller-Jensen, J. Löwe, K. Gerdes, *Mol. Microbiol.* **2008**, *68*, 720.
[32] M. Fornt-Suñé, G. L. Bermejo, M. Gil-Garcia, A. Aran, J. Garcia-Pardo, M. Martí, S. Ventura, *ACS Appl. Nano Mater.* **2024**, *7*, 6669.
[33] L. Cao, B. Coventry, I. Goreshnik, B. Huang, W. Sheffler, J. S. Park, K. M. Jude, I. Markovic, R. U. Kadam, K. H. G. Verschueren, K. Verstraete, S. T. R. Walsh, N. Bennett, A. Phal, A. Yang, L. Kozodoy, M. DeWitt, L. Picton, L. Miller, E.-M. Strauch, N. D. DeBouver, A. Pires, A. K. Bera, S. Halabiya, B. Hammerson, W. Yang, S. Bernard, L. Stewart, I. A. Wilson, H. Ruohola-Baker, et al., *Nature* **2022**, *605*, 551.
[34] L. Cao, I. Goreshnik, B. Coventry, J. B. Case, L. Miller, L. Kozodoy, R. E. Chen, L. Carter, A. C. Walls, Y.-J. Park, E.-M. Strauch, L. Stewart, M. S. Diamond, D. Veesler, D. Baker, *Science* **2020**, *370*, 426.
[35] J. B. Case, R. E. Chen, L. Cao, B. Ying, E. S. Winkler, M. Johnson, I. Goreshnik, M. N. Pham, S. Shrihari, N. M. Kafai, A. L. Bailey, X. Xie, P.-Y. Shi, R. Ravichandran, L. Carter, L. Stewart, D. Baker, M. S. Diamond, *Cell Host Microbe* **2021**, *29*, 1151.
[36] M. Gil-Garcia, S. Ventura, *Front. Bioeng. Biotechnol.* **2021**, *9*, 734068.
[37] M. Behbahanipour, R. Benoit, S. Navarro, S. Ventura, *ACS Appl. Mater. Interfaces* **2023**, *15*, 11444.
[38] J. Alves, L. Engel, R. de Vasconcelos Cabral, E. L. Rodrigues, L. de Jesus Ribeiro, L. M. Higa, O. da Costa Ferreira Júnior, T. M. P. P. Castiñeiras, I. de Carvalho Leitão, A. Tanuri, S. A. Goueli, H. Zegzouti, *Sci. Rep.* **2021**, *11*, 18428.
[39] P. Kallem, H. Hegab, H. Alsafar, S. W. Hasan, F. Banat, *Emerg. Microbes Infect.* **2023**, *12*, 2222850.
[40] K.-H. Chan, S. Sridhar, R. R. Zhang, H. Chu, A. Y.-F. Fung, G. Chan, J. F.-W. Chan, K. K.-W. To, I. F.-N. Hung, V. C.-C. Cheng, K.-Y. Yuen, *J. Hosp. Infect.* **2020**, *106*, 226.
[41] E. Forés, S. Bofill-Mas, M. Itarte, S. Martínez-Puchol, A. Hundesa, M. Calvo, C. M. Borrego, L. L. Corominas, R. Girones, M. Rusiñol, *Sci. Total Environ.* **2021**, *768*, 144786.
[42] Y. Isaka, T. Yoshiya, C. Ono, A. Uchiyama, H. Hirata, S. Hamaguchi, S. Kutsuna, Y. Takabatake, R. Saita, T. Yamada, A. Takahashi, M. Yamato, Y. Nohara, S. Tsuda, I. Anzai, T. Kimura, Y. Takeda, K. Tomono, Y. Matsuura, *Clin. Exp. Nephrol.* **2023**, *27*, 279.
[43] J. L. Watson, D. Juergens, N. R. Bennett, B. L. Trippe, J. Yim, H. E. Eisenach, W. Ahern, A. J. Borst, R. J. Ragotte, L. F. Milles, B. I. M. Wicky, N. Hanikel, S. J. Pellock, A. Courbet, W. Sheffler, J. Wang, P. Venkatesh, I. Sappington, S. V. Torres, A. Lauko, V. De Bortoli, E. Mathieu, S. Ovchinnikov, R. Barzilay, T. S. Jaakkola, F. DiMaio, M. Baek, D. Baker, *Nature* **2023**, *620*, 1089.
[44] S. Vázquez Torres, P. J. Y. Leung, P. Venkatesh, I. D. Lutz, F. Hink, H.-H. Huynh, J. Becker, A. H.-W. Yeh, D. Juergens, N. R. Bennett,

A. N. Hoofnagle, E. Huang, M. J. MacCoss, M. Expòsit, G. R. Lee, A. K. Bera, A. Kang, J. De La Cruz, P. M. Levine, X. Li, M. Lamb, S. R. Gerben, A. Murray, P. Heine, E. N. Korkmaz, J. Nivala, L. Stewart, J. L. Watson, J. M. Rogers, D. Baker, *Nature* **2024**, *626*, 435.

[45] C. A. Schneider, W. S. Rasband, K. W. Eliceiri, *Nat. Methods* **2012**, *9*, 671.

[46] V. M. Corman, O. Landt, M. Kaiser, R. Molenkamp, A. Meijer, D. K. Chu, T. Bleicker, S. Brünink, J. Schneider, M. L. Schmidt, D. G. Mulders, B. L. Haagmans, B. Vander Veer, S. Van der Brink, L. Wijsman, G. Goderski, J.-L. Romette, J. Ellis, M. Zambon, M. Peiris, H. Goossens, C. Reusken, M. P. Koopmans, C. Drosten, *Eurosurveillance* **2020**, *25*, 2000045.

[47] P. Scotti, **2013**, http://doi.org/10.13140/2.1.4777.1209.